

# Theory of an autonomous quantum heat engine based on superconducting electric circuits with non-Markovian heat baths

Miika Rasola,<sup>1,\*</sup> Vasilii Vadimov,<sup>1,†</sup> Tuomas Uusnäkki,<sup>1</sup> and Mikko Möttönen<sup>1,2,‡</sup>

<sup>1</sup>*QCD Labs, QTF Centre of Excellence,  
Department of Applied Physics, Aalto University,  
P.O. Box 13500, FI-00076 Aalto, Finland*

<sup>2</sup>*QTF Centre of Excellence, VTT Technical Research Centre of Finland Ltd.,  
P.O. Box 1000, 02044 VTT, Finland*

(Dated: February 13, 2025)

# Abstract

We propose and theoretically analyze a realistic superconducting electric circuit that can be used to realize an autonomous quantum heat engine in circuit quantum electrodynamics. Using a quasiclassical, non-Markovian theoretical model, we demonstrate that coherent microwave photon generation can emerge solely from heat flow through the circuit and its nonlinear internal dynamics. The predicted generation rate is sufficiently high for experimental observation in circuit quantum electrodynamics, making this work a significant step toward the first experimental realization of an autonomous quantum heat engine in superconducting circuits.

## I. INTRODUCTION

Superconducting quantum circuits provide one of the most versatile platforms for experimentally realizing various quantum technologies and devices [1]. The field of quantum microwave engineering, serving a purpose beyond fundamental research with the goal of realizing useful quantum devices [1, 2], has already produced numerous groundbreaking results in quantum computation [3–7], communication [8–11], simulation [12–18], and sensing [19–26].

As quantum technologies evolve further, the necessity for understanding thermodynamics at the quantum level becomes increasingly urgent. Quantum thermodynamics [27–29] seeks to extend the theories of classical thermodynamics into the domain of single quantum systems in order to improve our understanding of microscopic, out-of-equilibrium systems with heat flows. The theoretical concept of a thermodynamic cycle, along with the heat engine that implements it, has been foundational to thermodynamics since its inception. Thus, it is no wonder that they remain indispensable in the quantum era.

Although microwave quantum engineering has led to significant breakthroughs in recent decades, to date, there has been only one reported experimental realization of a quantum heat engine (QHE) in superconducting quantum circuits [30]. In contrast, there have been

---

\* Corresponding author.

miika.rasola@aalto.fi

† Corresponding author.

vasilii.1.vadimov@aalto.fi

‡ Corresponding author.

mikko.mottonen@aalto.fi

numerous experimental demonstrations of QHEs in microscopic atomic devices, such as single trapped ions [31], a spin coupled to single-ion motion [32, 33], nitrogen-vacancy center interacting with a light field [34], nuclear magnetic resonance [35, 36], and large quasi-spin states of Cesium impurities immersed in an ultracold Rubidium bath [37]. There exists, however, a substantial amount of experimental studies about heat conduction and thermodynamics in superconducting circuits providing prospects for demonstrating QHEs [38–43].

A particularly interesting class of thermal devices operating at the single quantum level is the set of devices capable of autonomous operation, only utilizing the flow of heat as power input in order to perform useful work. All of the above-cited thermal machines are inherently not autonomous because their thermodynamic cycles need to be driven by some type of external control. In this case, it is very difficult to extract, or even directly observe, the work produced by the heat engine as it only exists superimposed on a macroscopic external control field.

Although superconducting quantum circuits have yet to conquer the field of quantum thermal machines, we believe they offer a promising platform for realizing the first autonomous QHE. In this article, we build upon our previous work [44], where we proposed a general-level theoretical approach for realizing an autonomous QHE using an arbitrary system governed optomechanical Hamiltonian [45, 46]. Here, we focus on a realistic superconducting circuit and derive an in-depth theoretical model from first principles, explicitly linking it to the physical quantities defining the electric circuit. Furthermore, we will show that in a carefully constructed superconducting circuit, a resonator acting as the controller of the cycle can exhibit negative internal dissipation — i.e. coherent generation of microwave photons — arising solely from the internal dynamics and the heat flow through the circuit.

It should be mentioned that various theoretical proposals of QHEs both in optomechanical systems and quantized superconducting circuits from other authors precede this work. References. [47–49] extensively analyze the possibility of realizing a coherently driven quantum Otto cycle in an optomechanical system, whereas Refs. [50–52] utilize optomechanical systems, but rely on periodic incoherent thermal drives. Hardal et al. [52] even propose a device based on superconducting circuits, but leave the discussion on a very general level without specifying the circuit. Further, Refs. [53–55] study theoretical models of autonomous QHEs on the level of Markovian master equations. In contrast to these high-level theoretical proposals, we take the discussion closer to a readily designed device by analyzing a realis-

tic circuit starting from the physical quantities defining the circuit. Further, the proposed device will be a fully autonomous QHE without any periodic thermal pumping or coherent drive whatsoever. Finally, as opposed to the other approaches, our theoretical description is non-Markovian taking into account the peaked shape of the reservoir spectra, which, in our view, is required to satisfactorily describe an autonomous QHE.

## II. DEVICE

### A. The circuit

Before delving into the theoretical details, let us first specify the circuit. In Fig. 1 we present a lumped element circuit model for the QHE and assign the required physical quantities. As can be seen from Fig. 1, the QHE circuit consists of four LC resonators denoted as A, B, C, and H, each comprising of a capacitance,  $C_i$ , and an inductance,  $L_i$ , with  $i = a, b, c, h$ . In the following, we shall introduce the notation of using the subscripts “h” and “c” for “hot” and “cold”, respectively. Resonators C and H, collectively referred to as the filters, contain dissipative elements at temperatures  $T_c < T_h$ , respectively, and will act as the non-Markovian heat reservoirs with Lorentzian-shaped power spectral densities. The filters are linearly coupled to resonator A via the coupling capacitances  $C_{ha}$  and  $C_{ca}$ . The core of the QHE is formed by the coupled system of resonators A and B where the nonlinear coupling implemented by SQUID enables the performance of the heat engine. The inductor of resonator A is grounded through a symmetric SQUID, such that part of the inductor of resonator B becomes part of the SQUID loop, establishing the nonlinear coupling between A and B. In the context of the heat engine, resonator A can be viewed as the working fluid, while resonator B acts as a flywheel that facilitates work output. As an intuition providing notion, an unequivocal analogue to internal combustion engine emerges when one considers resonator A as the piston of the engine moving within the cylinder and resonator B as the combination of the crank shaft and the flywheel.

In addition to the physical structure and quantities, we define six flux node variables [56, 57], one for each resonator plus two auxiliary node variables,  $\varphi_s$  and  $\varphi_g$ , for the purpose of modelling the SQUID-mediated coupling correctly. For now, we divide the field in resonator B into two components, but go on to derive an effective field approach unifying the two fields

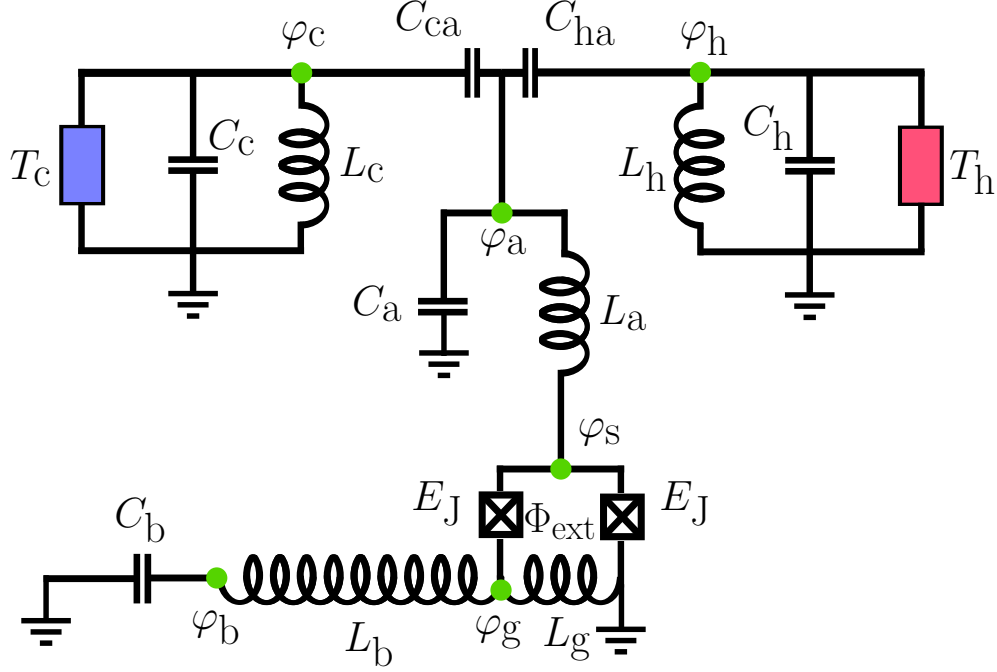


FIG. 1. Lumped element circuit model of the quantum heat engine. The heat engine circuit consists of four LC resonators denoted as A, B, C, and H. The main capacitances and inductances of the resonators are denoted as  $C_i$  and  $L_i$ , respectively, with  $i = a, b, c, h$ . The capacitances  $C_{ca}$  and  $C_{ha}$  couple resonator A to resonators C and H, respectively. Resonators C and H contain dissipative elements, indicated by the blue and red boxes, maintained at temperatures  $T_c$  and  $T_h$ , respectively. The Josephson junctions in the symmetric SQUID loop both have a Josephson energy of  $E_J$  while  $\Phi_{\text{ext}}$  denotes the external magnetic flux threading the SQUID loop. Additionally, a small piece of inductor directly connected to resonator B with the inductance  $L_g$  forms a part of the SQUID loop, through which resonator B is also grounded. Finally, we indicate the circuit nodes with green dots, and assign a flux variable  $\varphi_i$ , with  $i = a, b, c, h, s, g$ , for each node.

into a single equation of motion. The field  $\varphi_g$  can be thought of as the coupling field — the part of  $\varphi_b$  that couples to the field  $\varphi_s$ . Similarly,  $\varphi_s$  represents a small deviation from  $\varphi_a$ , separated by the inductance  $L_a$ , that couples to  $\varphi_g$  via the SQUID. In the following, we will rigorously derive the equations of motion for these fields and go on to show that the mode in resonator B can undergo coherent generation arising solely from the internal dynamics of the device and the heat flow from the hot to the cold reservoir.

## B. Initial assumptions and the recipe for solution

As the final step in our preparation, we will make some initial assumptions about the system's parameters necessary for achieving the desired QHE dynamics and outline the approach for modelling the system. The primary goal of this circuit is to achieve a dynamic where resonator A undergoes a cycle analogous to the quantum Otto cycle [27, 58] driven by the field amplitude of resonator B. This concept, along with most of the assumptions made here, has been thoroughly discussed phenomenologically in Ref. [44]. Therefore, we will simply list the assumptions here without delving into detailed reasoning.

The first requirement, as previously mentioned, is of course the presence of heat reservoirs at different temperatures:  $T_c < T_h$ . We have already assigned angular frequencies for the filter resonators, but, crucially, the hot filter must have the higher frequency. In Ref. [44], the following condition for the angular frequency of resonator A is set: in the operational mode, the angular frequency of the working fluid,  $\omega'_a$ , must lie between the filter frequencies, resulting in the condition  $\omega_c < \omega'_a < \omega_h$ . In the current circuit,  $\omega'_a$  is an effective angular frequency of the subcircuit consisting of  $C_a$ ,  $L_a$  and the SQUID loop. By virtue of the SQUID, this frequency becomes flux-tunable and must be tuned to the suitable value by the external flux  $\Phi_{\text{ext}}$ . Below, we find an approximate expression for  $\omega'_a$  and show that, while the exact formulation of this condition differs slightly within the framework used here, its fundamental principle remains unchanged. For successful tuning, the frequency gap between the filter resonators must exceed the capacitive coupling strength between the filters and resonator A arising from  $C_{ca}$  and  $C_{ha}$ . Lastly, we impose the condition that the angular frequency of resonator B must be significantly lower than that of the other resonators:  $\omega_b \ll \omega_c < \omega_a < \omega_h$  [44].

Our goal is to theoretically show that the internal dynamics of the circuit can lead to observable generation of coherent microwave photons in resonator B. In order to achieve this, we identify three characteristic time scales in the system: the short time scale governed by the high frequencies  $\omega_a$ ,  $\omega_h$ , and  $\omega_c$ , the intermediate scale associated with the frequency  $\omega_{b/g}$ , and the long time scale, determined by the rate at which the average occupation or field amplitude in resonator B changes — that is, the rate of generation. We shall further assume that the rate of generation is considerably lower than the frequency of resonator B,  $\omega_b$ , which effectively allows using the WKB approximation [59] for the resonator mode  $\phi_b$ .

Based on this assumption, we will systematically eliminate all other degrees of freedom, but the mode in resonator B, ultimately arriving at an equation of motion for the amplitude and phase of the mode in resonator B.

### III. THEORY

#### A. Equations of motion

Excluding the SQUID and the dissipative components, the classical Lagrangian for the circuit described above, with the definitions used in Fig. 1, is given as

$$\mathcal{L}_R = \frac{C_{\Sigma a} \dot{\varphi}_a^2}{2} - \frac{(\varphi_a - \varphi_s)^2}{2L_a} + \frac{C_b \dot{\varphi}_b^2}{2} - \frac{(\varphi_b - \varphi_g)^2}{2L_b} + \sum_f \left[ \frac{C_{\Sigma f} \dot{\varphi}_f^2}{2} - \frac{\varphi_f^2}{2L_f} + C_{fa} \dot{\varphi}_a \dot{\varphi}_f \right], \quad (1)$$

where we define the capacitance sums  $C_{\Sigma a} = C_a + C_{ha} + C_{ca}$  and  $C_{\Sigma f} = C_f + C_{fa}$ . The Lagrangian including the elements in the SQUID loop endowing the coupling between resonators A and B is given as

$$\mathcal{L}_S = -\frac{\varphi_g^2}{2L_g} + E_J \cos\left(\frac{2\pi\varphi_s}{\Phi_0}\right) + E_J \cos\left(\frac{2\pi}{\Phi_0} [\varphi_s - \varphi_g - \Phi_{\text{ext}}]\right), \quad (2)$$

where  $E_J = I_c \Phi_0 / (2\pi)$  is the Josephson energy of the junctions with the critical current  $I_c$  and the magnetic flux quantum  $\Phi_0 = \pi \hbar / e$ , defined by the reduced Planck constant,  $\hbar$ , and the electron charge,  $e$ . The total Lagrangian of the circuit without any approximations, is now given by the sum  $\mathcal{L} = \mathcal{L}_R + \mathcal{L}_S$ .

Typically, the trigonometric potential in the SQUID Lagrangian is Taylor expanded up to the first non-linear correction. Before doing this, however, we need to ensure that the field variables in the cosine are sufficiently small. To this end, we shall find the potential minimum of the potential energy related to the above SQUID loop Lagrangian (2), and shift the fields by this offset. This calculation and the following series expansion along with the appropriate approximations are carried out in Appendix A. The approximated SQUID loop Lagrangian now reads

$$\mathcal{L}'_S = -\left(\frac{1}{2L_J} + \frac{1}{2L_g}\right) \varphi_g^2 - \frac{\varphi_s^2}{L_J} + g_0^2 \varphi_g \varphi_s^2, \quad (3)$$

where we define the optomechanical coupling constant and the Josephson inductance, re-

spectively, as

$$g_0^2 = \frac{4I_c \pi^2}{\Phi_0^2} \sin\left(\frac{\pi}{\Phi_0} \varphi_g^{(0)}\right), \quad (4)$$

$$L_J^{-1} = \frac{4I_c \pi}{\Phi_0} \cos\left(\frac{\pi}{\Phi_0} \varphi_g^{(0)}\right), \quad (5)$$

where  $\varphi_g^{(0)}$  is the offset of the potential minimum given by the equation

$$\frac{\varphi_g^{(0)} - \Phi_{\text{ext}}}{L_g} + 2I_c \sin\left(\frac{\pi}{\Phi_0} \varphi_g^{(0)}\right) = 0. \quad (6)$$

The above equation is transcendental and in general needs to be solved numerically. We notice, that this equation has a single solution when  $I_c \gg L_g$ , which will be satisfied easily in our circuit. This approximate Lagrangian now replaces the full SQUID loop Lagrangian (2), while the resonator Lagrangian (1) retains its original form.

The equations of motion are obtained by direct application of the Euler–Lagrange equation:

$$\ddot{\varphi}_a + \omega_a^2 (\varphi_a - \varphi_s) + \sum_f \kappa_{fa} \ddot{\varphi}_f = 0, \quad (7a)$$

$$\frac{\varphi_a - \varphi_s}{L_a} - \frac{2\varphi_s}{L_J} + 2g_0^2 \varphi_s \varphi_g = 0, \quad (7b)$$

$$\ddot{\varphi}_b + \frac{\varphi_b - \varphi_g}{C_b L_b} = 0, \quad (7c)$$

$$\left(\frac{1}{L_b} + \frac{1}{L_g} + \frac{1}{L_J}\right) \varphi_g - \frac{\varphi_b}{L_b} - g_0^2 \varphi_s^2 = 0, \quad (7d)$$

$$\ddot{\varphi}_f + \omega_f^2 \varphi_f + 2\gamma_f \dot{\varphi}_f + \kappa_f \ddot{\varphi}_a = \xi_f(t), \quad (7e)$$

where  $f = h, c$  for hot and cold filter resonator, respectively, we define the angular frequencies  $\omega_a = 1/\sqrt{C_{\Sigma a} L_a}$  and  $\omega_f = 1/\sqrt{C_{\Sigma f} L_f}$ , and the dimensionless coupling constants  $\kappa_{fa} = C_{fa}/C_{\Sigma a}$  and  $\kappa_f = C_{fa}/C_{\Sigma f}$ ,  $\gamma_f = 1/(R_f C_{\Sigma f})$  is the filter dissipation rate and  $\xi_f(t)$  is the noise source function due to the thermal environment [60], characterized by the spectral density:

$$\langle \xi_f(\omega) \xi_f^*(\omega') \rangle = S(\omega) \delta(\omega + \omega') = \hbar \omega \gamma_f \coth\left(\frac{\hbar \omega}{2k_B T_f}\right) \delta(\omega + \omega'), \quad (8)$$

where  $T_f$  is the temperature of the heat reservoir, and  $k_B$  is the Boltzmann constant. Above, we formally define  $\gamma_f$  through the resistance  $R_f$ , serving as the source of thermal noise in the filter resonator. Since this resistance can be freely chosen,  $\gamma_f$  is effectively a free parameter.



Therefore, moving forward, we will treat  $\gamma_f$  as a fundamental parameter and disregard the resistance.

As stated earlier, our primary focus lies in the evolution of the mode  $\varphi_b$ . To this end, we shall reduce the above set of equations by integrating out certain of the degrees of freedom. First, we will solve  $\varphi_g$  from Eq. (7d) in the time domain and insert the solution into Eqs. (7b) and (7c). In accordance with the approximations in Appendix A will drop the resulting third order terms. Next, we will solve  $\varphi_f$  from Eq. (7e) via Fourier transformation and plug the solution into the Fourier transformed Eq. (7a). The resulting equation for  $\varphi_a$  in Fourier space is then solved, and the solution is substituted back into Eq. (7b), thus reducing number of equations to two. Finally, we redefine the units in the two remaining equations to render the field variables dimensionless. The details of the above derivation can be found in Appendix B. After these steps, we can finally write down the equations of motion governing the time evolution of the fields  $\phi_b$  and  $\phi_s$ :

$$\omega_s^2 \phi_s(t) + 2g_s^2 \phi_s(t) \phi_b(t) - \int_{-\infty}^{\infty} d\tau \mathcal{K}(t - \tau) \phi_s(\tau) = \xi(t), \quad (9)$$

$$\ddot{\phi}_b(t) + \omega_b^2 \phi_b(t) - g_b^2 \phi_s^2(t) = 0, \quad (10)$$

where the angular frequencies are defined as  $\omega_s^2 = (1 + 2L_a/L_J) \omega_a^2$  and  $\omega_b^2 = (1 - N_L)/(L_b C_b)$ , with  $N_L = 1 + L_b/L_g + L_b/L_J$ , and the nonlinear coupling constants are given by

$$g_s^2 = \frac{\Phi_0 g_0^2}{\pi C_{\Sigma a} N_L}, \quad g_b^2 = \frac{\Phi_0 g_0^2}{\pi C_b N_L}. \quad (11)$$

The total noise source function  $\xi(\omega)$  and the memory kernel  $\mathcal{K}(\omega)$  are defined, in the frequency domain, as

$$\xi(\omega) = \frac{\omega_a^2 \sum_f \eta_f(\omega) \xi_f(\omega)}{\omega_a^2 - \omega^2 \left(1 + \sum_f \kappa_f \eta_f(\omega)\right)}, \quad (12)$$

$$\mathcal{K}(\omega) = \frac{\omega_a^4}{\omega_a^2 - \omega^2 \left(1 + \sum_f \kappa_f \eta_f(\omega)\right)}, \quad (13)$$

$$\eta_f(\omega) = \frac{\kappa_{fa} \omega^2}{\omega_f^2 - \omega^2 - 2i\gamma_f \omega}. \quad (14)$$

See Appendix B for the details of obtaining these definitions.

We have now reduced the original set of equations into two equations by integrating out the noise-driven filter modes along with  $\varphi_a$ , and consolidating the two modes within

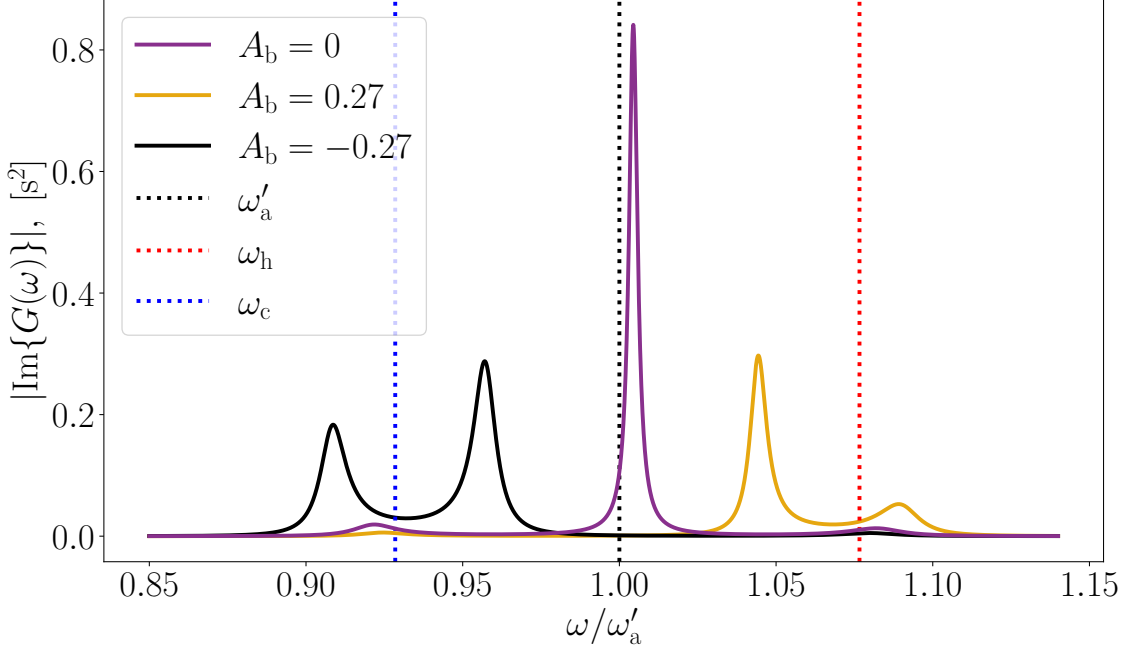


FIG. 2. Time-independent Green’s function as a function of  $\omega$  in frequency domain at different values of  $A_b$ . Red and blue vertical dashed lines represent the bare frequencies of hot and cold filters, respectively, while the black dashed line shows the flux tunable frequency defined in the main text. We demonstrate the modulation due to  $\phi_b$  by plotting the Green’s function at  $A_b \pm 0.27$ . The parameters used for this plot are listed in Table I.

resonators B. We are left with Eq. (9), describing the dynamics at the node coupling the SQUID to resonator A, and Eq. (10), governing the dynamics of resonator B. Note that Eq.(10) retains the form of a harmonic oscillator equation, while Eq. (9) is fully governed by the memory kernel  $\mathcal{K}(\omega)$  and the noise source  $\xi(\omega)$ . Let us finally define the effective frequency of the flux-tunable resonator consisting of resonator A and the SQUID termination, as depicted in Fig. 1. Using the above given external-flux dependent Josephson inductance, we can define  $\omega'_a = 1/\sqrt{C_{\Sigma a}(L_a + L_J/2)}$ , which is now the frequency that must be tuned to the operational range, given by  $\omega_c < \omega'_a < \omega_h$ , as mentioned in Sec. II.

Our next step is to integrate out the remaining high-frequency components in the system by solving Eq. (9) for  $\phi_s$ . Before attempting at a solution of Eq. (9), let us try to gain some intuition into the equation and the implied dynamics by examining its structure. By replacing the field  $\phi_b(t)$  with a time-independent constant amplitude  $A_b$ , we quickly recover

the time-independent Green's function for Eq. (9) in frequency domain:

$$G(\omega) = [\omega_s^2 + 2g_s^2 A_b - \mathcal{K}(\omega)]^{-1}. \quad (15)$$

In Fig. 2 we plot the absolute value of the imaginary part of the above Green's function at different values of  $A_b$ . We observe the peaks related to each of the modes  $\phi_a$ ,  $\phi_h$  and  $\phi_c$ , slightly offset from their estimated bare values due to coupling. As expected, the peak associated with  $\phi_a$  is by far the strongest, since the  $\phi_s$  is directly coupled to it by the inductance  $L_a$ , as seen from Fig. 1. The mode  $\phi_s$  serves as an auxiliary mode, housed by resonator A, to model the SQUID-mediated coupling between resonators A and B. Coupling to the filters is mediated by the mode  $\phi_a$ , and further weakened by the relatively weak capacitive coupling. We demonstrate the modulating effect of the field  $\phi_b$  on Eq. (9) by plotting the Green's function with  $A_b \pm 0.27$ . As alluded already in Sec. II, the phenomenological notion of  $\phi_b$  modulating the frequency of resonator A between the filter frequencies is clearly evinced here. Depending on the value of  $A_b$  the peak related to  $\phi_a$  moves closer to either of the filter frequencies. We also note that there is a slight repulsion to the filter frequency, which, in turn, moves further away.

## B. Finding the Green's function

Equation (9) is a time non-local integral equation with a peaked-spectrum noise function as the source term. We will therefore employ Green's function methods in order to find the solution for an arbitrary source. We will treat the left-hand side of the equation (9) as a differential operator, so that the Green's function obeys the following equation

$$[\omega_s^2 + 2g_s^2 \phi_b(t)] G(t, t') - \int_{-\infty}^{\infty} \mathcal{K}(t - \tau) G(\tau, t') d\tau = \delta(t - t'). \quad (16)$$

The above equation is challenging due to the time dependence of  $\phi_b(t)$ , and its explicit solution remains unavailable in general case. In order to work around this, we shall express the field variable  $\phi_b$  as

$$\phi_b(t) = 2A_b(t) \cos[\omega_b t + \theta_b(t)], \quad (17)$$

where  $A_b(t)$  and  $\theta_b(t)$  are the time-dependent amplitude and phase of the field, respectively. In the following computation, we invoke the approximation of slow time evolution of  $A_b(t)$

and  $\theta_b(t)$ . This is formally expressed as the assumption that the evolution rates are much lower than the inverse of the heat bath correlation time:  $\dot{A}_b, \dot{\theta}_b \ll \gamma_f$ . Practically, however, this simply means that we will ignore their time dependence, for now. To proceed, we transform the equation into Fourier space by writing the Green's function in a doubly Fourier-transformed form,

$$G(t, t') = \frac{1}{2\pi} \iint_{-\infty}^{\infty} G(\omega, \omega') e^{-i\omega t + i\omega' t'} d\omega d\omega', \quad (18)$$

and substitute it in Eq. (16) taking care of the time-dependent term of  $\phi_b$ . We arrive at the following equation

$$[\omega_s^2 - \mathcal{K}(\omega)] G(\omega, \omega') + 2g_s^2 A_b [e^{-i\theta_b} G(\omega - \omega_b, \omega') + e^{i\theta_b} G(\omega + \omega_b, \omega')] = \delta(\omega - \omega'). \quad (19)$$

To facilitate numerical solutions, let us reformulate the problem as a matrix equation. Specifically, we will look for solutions in the vicinity of multiples of the angular frequency,  $\omega_b$ , in Fourier space. To this end, we will express the Green's function in a form

$$G(\omega, \omega') = \sum_n G_n(\omega) \delta(\omega - \omega' - n\omega_b). \quad (20)$$

By substituting this ansatz into Eq. (19), one arrives at

$$\sum_n [P(\omega + n\omega_b) G_n(\omega) + R^*(\theta_b) G_{n-1}(\omega) + R(\theta_b) G_{n+1}(\omega)] = \delta_{n,0}, \quad (21)$$

where  $P(\omega) = \omega_s^2 - \mathcal{K}(\omega)$  and  $R(\theta_b) = 2g_s^2 A_b e^{i\theta_b}$ . This formulation produces a set of equations, with each index  $n$  corresponding to one equation. The entire set can be expressed as a matrix equation, which can be efficiently solved numerically by inverting the associated matrix (see Appendix C). By computing the matrix inversion to a sufficient degree in  $n$ , a large enough set of coefficients  $G_n(\omega)$  in the series representation of the Green's function can be determined, allowing for accurate evaluation of the Green's function. Once the Green's function is known, one can solve the equation (9) for an arbitrary source  $\xi(\tau)$ :

$$\phi_s(t) = \int_{-\infty}^{\infty} G(t', t) \xi(t') dt'. \quad (22)$$

### C. Averaging over noise and time

Considering equation (10) we note that it is actually not  $\phi_s$  that we are interested in, but rather its square. Further, as already mentioned, the characteristic frequency of the

oscillations of  $\phi_{s/a}$  are far off-resonant, and at a much higher frequency, as compared to the oscillations of  $\phi_b$ . Besides, in noisy systems, one is typically not interested in the noisy solutions, but rather in the expectation values of observables. With this in mind, we replace the  $\phi_s^2$  appearing in Eq. (10) by its noise expectation value, thus creating a noise averaged equation for field  $\phi_b$ :

$$\ddot{\phi}_b + \omega_b^2 \phi_b + 2\gamma_b \dot{\phi}_b - g_b^2 \langle \phi_s^2 \rangle_\xi(t) = 0, \quad (23)$$

where we have also introduced dissipation into the equation, determined by the dissipation rate  $\gamma_b$ , in order to study the effects of varying loss rates.

Next, we utilize the expression (17) once more by inserting it into the above equation, and time averaging over one period of the mode  $\phi_b$ . Here, we consider a single Fourier harmonic of  $\langle \phi_s^2 \rangle_\xi(t)$  resonant to the mode  $\phi_b$ . At this point, we invoke the final assumption regarding the time scales of the system: the field amplitude  $A_b(t)$  evolves slowly in time as compared to the oscillation frequency  $\omega_b$ . To simplify the equation and focus on the leading-order behaviour, we neglect all second derivatives, products of derivatives, and other small terms in the spirit of the WKB approximation [59]. Finally, we decompose the result into its real and imaginary components, yielding separate equations of motion for the amplitude and phase, respectively:

$$\dot{A}_b(t) + \gamma_b A_b + \frac{g_b^2}{2\omega_b} \text{Im} \left[ \langle \phi_a^2 \rangle_{\xi,t}(A_b, \theta_b) \right] = 0, \quad (24)$$

$$A_b(t) \dot{\theta}_b + \frac{g_b^2}{2\omega_b} \text{Re} \left[ \langle \phi_a^2 \rangle_{\xi,t}(A_b, \theta_b) \right] = 0, \quad (25)$$

where

$$\langle \phi_a^2 \rangle_{\xi,t}(A_b, \theta_b) = \frac{1}{4\pi^2} e^{i\theta_b} \int_{-\infty}^{\infty} \sum_n G_n(\omega) G_{n-1}^*(\omega) S(\omega) d\omega, \quad (26)$$

is given in terms of the Green's function coefficients  $G_n(\omega)$ . The details of this calculation, along with the associated approximations, are provided in Appendix D. This expression can be evaluated efficiently numerically by the method described above. The equations of motion Eqs. (24) and (25) govern the dynamics of resonator B at the slowest time scale in the circuit, we proceed with the analysis of their solution in the next Section.

## IV. RESULTS

As explained in the beginning, our primary focus is to determine whether the proposed circuit can induce coherent generation of photons in resonator B and to identify the conditions under which this occurs. Although solving Eq. (24) would have to be done numerically, its simple structure allows us to obtain certain results without explicitly solving the equation. By dividing the equation by  $A_b$ , we define the amplitude-dependent total dissipation rate as

$$\Gamma_{\text{tot}}(A_b, \theta_b) = \gamma_b + \frac{g_b^2}{2A_b\omega_b} \text{Im} \left[ \langle \phi_a^2 \rangle_{\xi,t} (A_b, \theta_b) \right]. \quad (27)$$

From this it is evident that when the total dissipation rate is positive, the amplitude will decay in time, whereas a negative total dissipation rate causes the amplitude to grow. This is the condition for coherent generation. Here, we refer to  $\gamma_b$  as the intrinsic dissipation rate, as it contains all the sources of dissipation, be it internal or external, apart from the effect of the average noise pressure induced by the coupling to resonator A. Additionally, we define the intrinsic quality factor as  $Q_b = \omega_b/\gamma_b$ .

TABLE I. Physical parameters of the circuit used in the simulations herein. In the first section, we list the elementary parameters of the circuit given in Fig. 1, while the second section gives the derivative parameters defined throughout the main text.

Elementary parameters				Derivative parameters			
$L_a$	0.55 nH	$C_a$	0.2 pF	$\omega_a/(2\pi)$	15 GHz	$\omega'_a/(2\pi)$	9.85 GHz
$L_h$	0.78 nH	$C_h$	0.29 pF	$\omega_h/(2\pi)$	10.6 GHz	$\omega_s/(2\pi)$	20.2 GHz
$L_c$	0.9 nH	$C_c$	0.34 pF	$\omega_c/(2\pi)$	9.15 GHz	$L_J$	1.36 nH
$L_b$	0.78 nH	$C_b$	134 pF	$\omega_b/(2\pi)$	386 MHz	$N_L$	0.071
$L_g$	96.5 pH	$C_{ha}$	8.1 fF	$\kappa_h$	0.028	$\kappa_{ha}$	0.04
$I_c$	0.8 $\mu$ A	$C_{ca}$	11.1 fF	$\kappa_c$	0.033	$\kappa_{ca}$	0.054
$T_c$	10 mK	$\gamma_{h/c}$	$\omega_{h/c}/103$	$g_0$	$44.5 \sqrt{A}/Wb$	$g_b$	$0.66 \times \omega_b$
$T_h$	300 mK	$\Phi_{\text{ext}}$	$0.5253 \times \Phi_0$	$\varphi_g^0$	$0.45 \times \Phi_0$	$g_s$	$0.43 \times \omega_a$

First and foremost, we should verify that there exists some set of parameters that enable negative total dissipation rate. In Fig. 3(a) we plot Eq. (27) as a function of  $A_b$  for various intrinsic quality factor values. Notably, the total dissipation rate can become locally negative

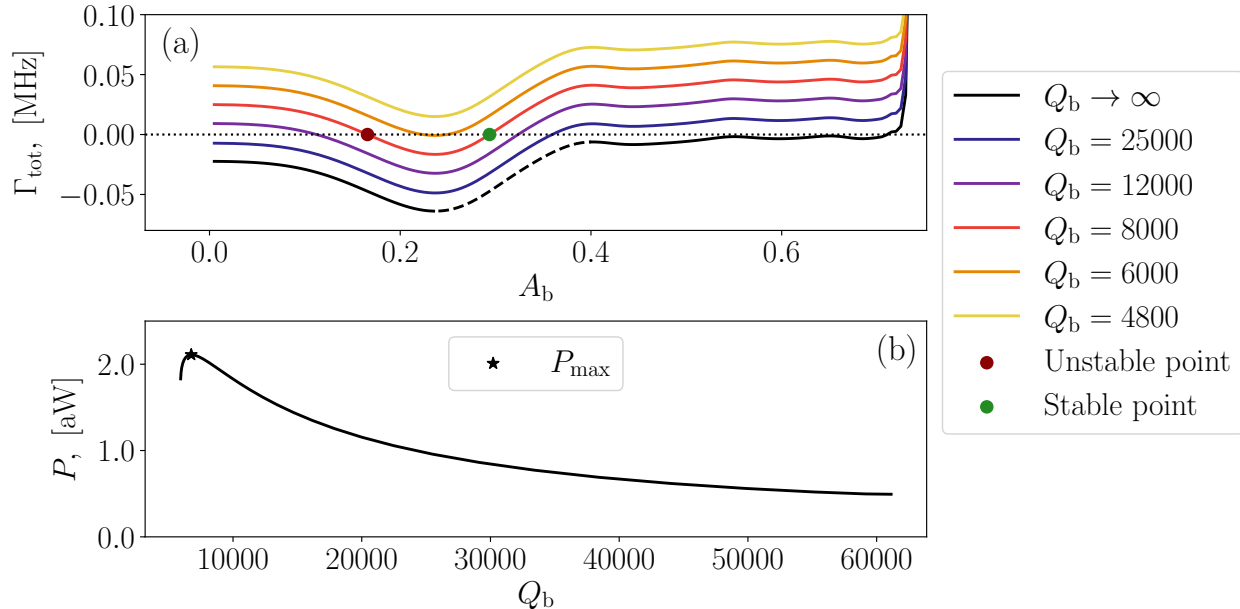


FIG. 3. (a) Total dissipation rate  $\Gamma_{\text{tot}}(A_b, \theta_b)$  as a function of field amplitude  $A_b$  at different intrinsic quality factors  $Q_b$ . The stable and unstable points are marked by the green (on the right) and the dark red (on the left) dots, respectively, on the  $Q_{\text{int}} = 8000$  curve. The dashed line segment on the  $Q_b \rightarrow \infty$  curve denotes the region where stable points may occur in the first generation valley. (b) Output power as a function of intrinsic quality factor, corresponding to the dashed line segment in panel (a). The star marks the location of maximum value of output power. The parameters used for computing the results are found in Table I.

within a certain range of  $A_b$ , depending on the intrinsic dissipation rate. Moreover, the total dissipation rate reaches large enough negative values to facilitate realistic experimental observation. This is evident from the curve corresponding to an intrinsic quality factor of  $Q_b = 6000$ , which still reaches negative values — this is a very low internal quality factor by modern standards [61–64]. It is worth mentioning that the parameters used here were not optimized for maximum negative dissipation rate, but for maximum power, as explained below. It is therefore possible to obtain even higher negative total dissipation rates. The parameters used for computing the results presented in Fig. 3 are listed in Table I. These parameters are applied to all subsequent computations unless otherwise stated.

To study the dynamics further, we use Eq. (24) to analyze how the field amplitude  $A_b$  evolves as a function of itself. Although there are multiple dips, or generation valleys, present in the curves in Fig. 3(a), let us only consider the first from left, as it is by far the

most prominent. Whenever the total dissipation rate is positive, the time derivative of the field amplitude  $A_b$  is negative resulting in the amplitude decreasing with time. Conversely, when the total dissipation rate becomes negative, the amplitude increases with time. Since the total dissipation rate is negative only within a finite generation valley, the amplitude increases until it reaches the point where  $\Gamma_{\text{tot}} = 0$ . Consequently, we can identify a stable point along the curve at the right-hand-side zero crossing. In addition, an unstable point may exist at the left-hand-side zero crossing, from where the amplitude will either decay to zero or start to increase towards the stable point. Both of the points are marked in Fig. 3(a). This is precisely what we wanted to demonstrate: the average noise pressure causing coherent generation arising solely from the internal dynamics of the system driven by thermal noise.

In order to estimate the output power of the device, let us assume that the internal losses of resonator B are negligible. This is reasonable, since, as mentioned above, the intrinsic quality factors considered here are much lower than the internal quality factors of state of the art resonators in circuit quantum electrodynamics (cQED) [61–65]. Consequently, resonator B loses energy at a rate  $\gamma_b$  to an external channel, for instance, a transmission line coupled to the resonator. Interpreting this out-flowing energy as the power output, we define the output power as

$$P = -\gamma_b E_b = -\gamma_b A_b^2 \frac{(1 - N_L)\Phi_0^2}{\pi^2 L_b}, \quad (28)$$

where  $E_b$  is the energy stored in the resonator B. Based on this, we can compute the attainable output power for all possible stable points by finding the pairs of intrinsic quality factor  $Q_b$  and field amplitude  $A_b$  that satisfy the condition  $\Gamma_{\text{tot}} = 0$ , and are stable points. This is demonstrated in Figs. 3(a)-(b), where panel (b) shows the power as a function of  $Q_b$ , determined in the range of possible stable points in the first generation valley, depicted in panel (a). Finally, we note that because of the  $A_b^2$ -dependence of power the parameters yielding maximal power output might be different from those yielding the maximal negative total dissipation.

In addition to showing that the device can reach a stable point of operation where coherent generation occurs, it is enlightening to examine how varying the device parameters influences the generation rate. Let us study this by performing a some of parameter sweeps, keeping all other parameters at fixed values given in Table I, while varying one parameter at a time.



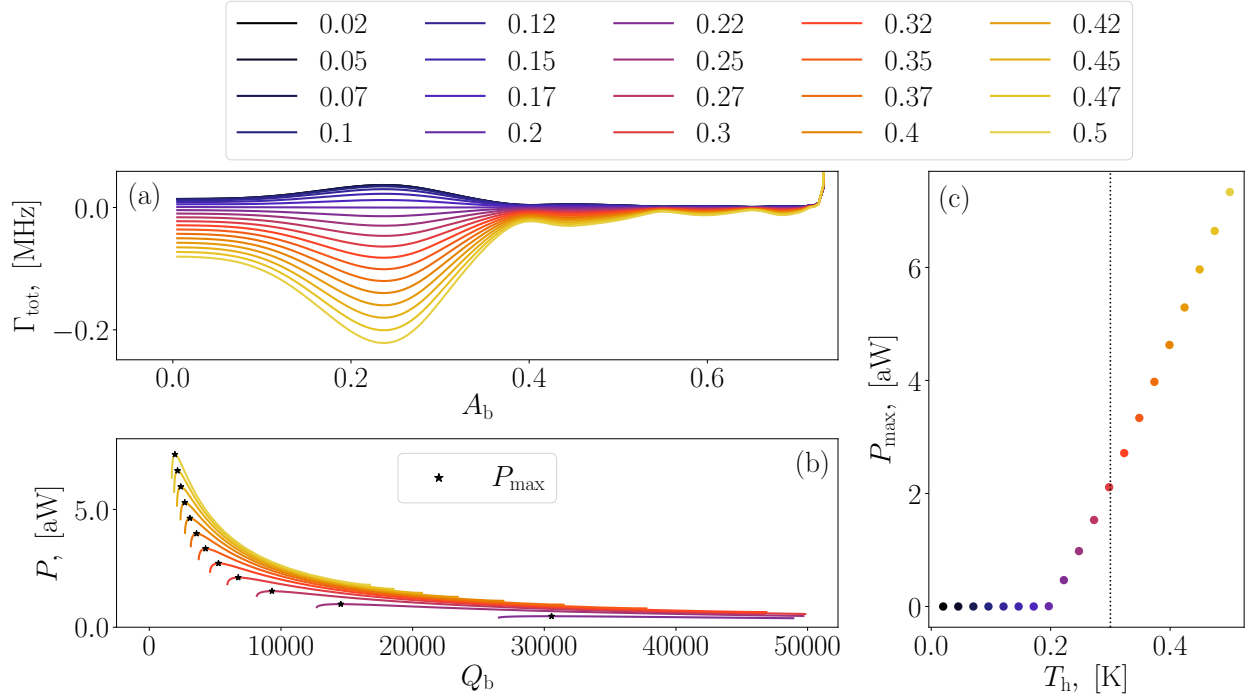


FIG. 4. (a) Total dissipation rate  $\Gamma_{\text{tot}}(A_b, \theta_b)$  as a function of field amplitude  $A_b$  at various hot bath temperatures  $T_h$ . (b) Output power as a function of intrinsic quality factor as determined from the possible stable points of the first generation valley. Note that curves below  $T_h = 200$  mK do not exhibit a negative total dissipation. (c) Maximum attainable output power as a function of  $T_h$ , determined by the points marked in panel (b) with the dotted vertical line marking the value of  $T_h$  given in Table I. The values in the legend are in units of kelvin. The fixed parameters used for computing these results are found in Table I.

Perhaps the most fundamental parameter to vary is the temperature of the hot heat bath. In Fig. 4(a) we plot the total dissipation rate with  $\gamma_b = 0$  as a function of field amplitude at different hot reservoir temperatures while keeping the cold reservoir at  $T_c = 10$  mK. In Fig. 4(b) we plot the power as a function of  $Q_b$ , inferred from the data of panel (a) via the method explained above. Finally, in panel Fig. 4(b) we show the maximum values of output power as a function of  $T_h$ . As expected, the generation valley deepens as a function of increasing temperature and maximum power increases monotonically accordingly, as seen from panel (b) and (c) of Fig. 4. We note that there seems to exist a threshold temperature, under which generation cannot occur. For the parameters used here, the threshold temperature is found at around  $T_h = 200$  mK. Under this temperature, the total

dissipation curve does not exhibit any valleys extending below the zero. The threshold is attributed the zero point fluctuations limiting the minimum of the quantum thermal noise spectral density at temperature close to zero, as seen from the  $\coth(1/T_{h/c})$  dependence in Eq. (12). Notice that form of the curve traced by the dots in Fig. 4(c) is qualitatively similar to the function  $\coth(1/T_h)$ .

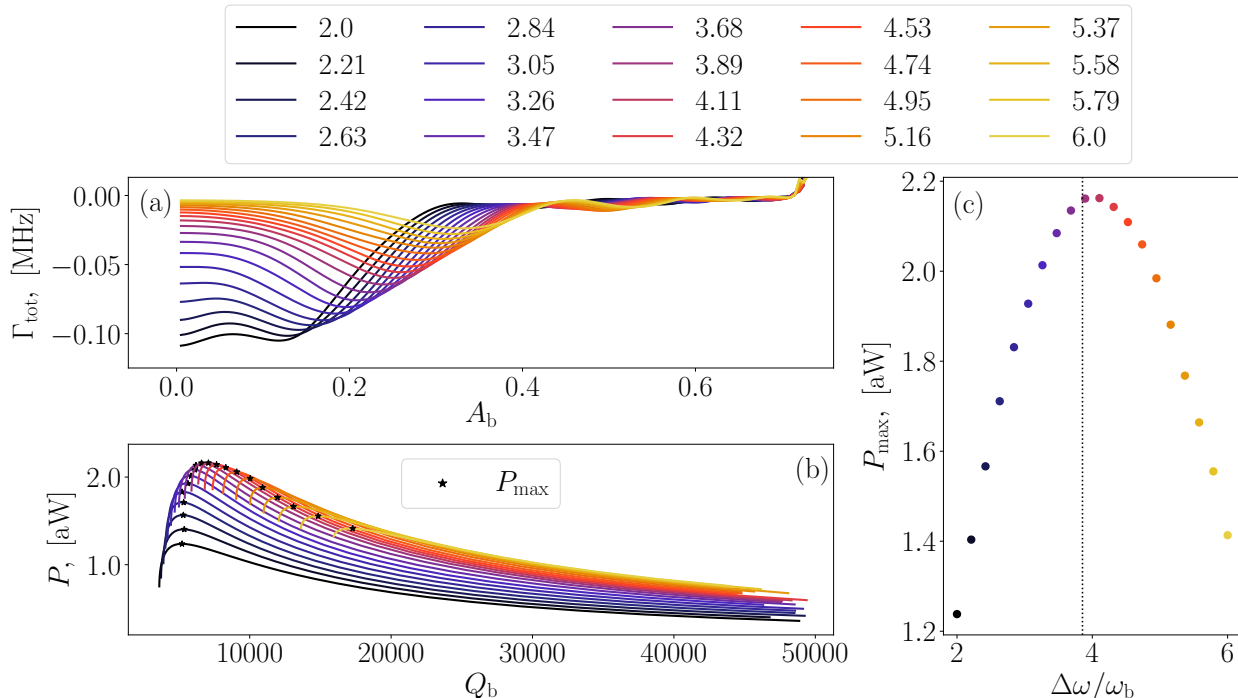


FIG. 5. (a) Total dissipation rate  $\Gamma_{\text{tot}}(A_b, \theta_b)$  as a function of field amplitude  $A_b$  at various filter resonator frequency differences  $\Delta\omega = \omega_h - \omega_c$ . (b) Output power as a function of intrinsic quality factor as determined from the possible stable points of the first generation valley. (c) Maximum attainable output power as a function of  $\Delta\omega$ , determined by the points marked in panel (b), with the dotted vertical line marking the value of  $\Delta\omega$  given in Table I. The values in the legend are in units of  $\omega_b$ . The fixed parameters used for computing these results are found in Table I.

Two parameters that acutely effect the performance of the heat engine are the centre frequencies of the heat reservoirs, specifically the frequency difference  $\Delta\omega = \omega_h - \omega_c$ . In Fig. 5(a) we plot the total dissipation rate with  $\gamma_b = 0$  as a function of field amplitude at various frequency differences  $\Delta\omega$ . Further, we infer the attainable power output as a function of  $Q_b$  in panel (b), and the maximum of power output as a function of  $\Delta\omega$  in panel (c), exactly the same way as before. One might expect that increasing  $\Delta\omega$  would always lead

to an equilibrium with higher field amplitude  $A_b$ , thus translating into a monotonously increasing output power as a function of  $\Delta\omega$  [44]. We note, however, that this is not the case here. Rather, the optimal value seems to be very close to  $\Delta\omega = 4\omega_b$ , and the output power falls off rapidly in both directions, as seen from Fig. 5(c). The assumption that increasing  $\Delta\omega$  increases the field amplitude  $A_b$  required to reach a stable is correct, though, as seen from panel (a). The generation valley just diminishes faster causing the generation rate to fall off. This shows that the device is relatively sensitive to the chosen parameters — a change of only 7% in the frequency of a filter resonator can cut the output power by almost half.

### A. Quantum disadvantage?

Let us revisit the temperature dependence of the hot heat bath here. Above we alluded that the threshold temperature for generation should be the consequence of the temperature dependence of the quantum thermal noise function, given by Eq. (8). In order to highlight the quantum nature of noise, and investigate the implications of that, we repeat the computation done for Fig. 4 with the classical thermal noise function. The classical thermal noise function is obtained as the high temperature limit of the quantum version:

$$S_f(\omega) = \hbar\omega\gamma_f \coth\left(\frac{\hbar\omega}{2k_B T_f}\right) \approx 2\gamma_f k_B T_f. \quad (29)$$

This will be the only change as compared to the results in Fig. 4, everything else is identical.

In Fig. 6 we plot the results of the the above computation in the familiar format at various hot bath temperatures. In panel (a) plot the total dissipation rate  $\Gamma_{\text{tot}}(A_b, \theta_b)$  as a function of the field amplitude  $A_b$ , while panel (b) shows the output power as a function of the intrinsic quality factor. Additionally, in panel (c) we show the maximum values of output power as a function of  $T_h$ . From Fig. 6(c) we immediately notice that the power with classical thermal noise is significantly higher than in the quantum case. Further, we observe that the initial plateau observed in Fig. 4(c) has disappeared, and the maximum power increases linearly with temperature of the hot bath. Thus, in the classical case, there is generation even with a tiny temperature separation. This behaviour is attributed to the form of the thermal noise function — the classical thermal noise function has linear temperature dependence reaching zero in the zero-temperature limit, while the quantum

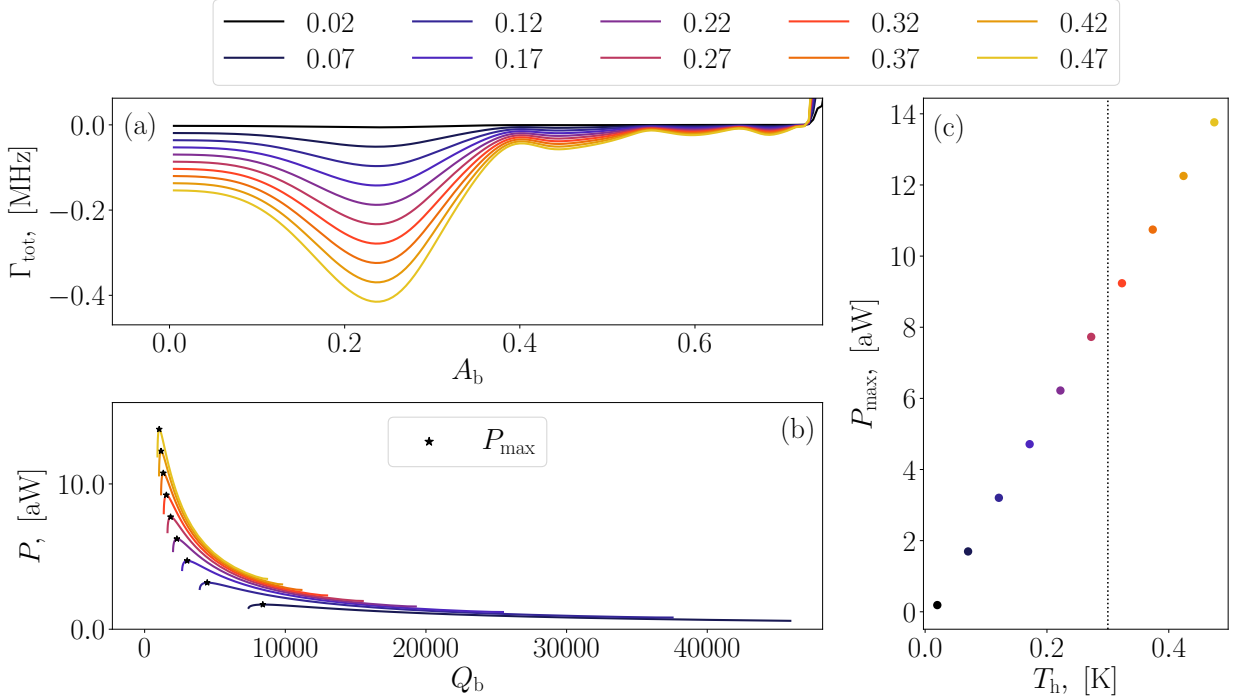


FIG. 6. Results in Fig. 4 reproduced using classical noise, characterised by Eq. (29). (a) Total dissipation rate  $\Gamma_{\text{tot}}(A_b, \theta_b)$  as a function of field amplitude  $A_b$  at various hot bath temperatures  $T_h$ . (b) Output power as a function of intrinsic quality factor as determined from the possible stable points of the first generation valley. (c) Maximum attainable output power as a function of  $T_h$ , determined by the points marked in panel (b) with the dotted vertical line marking the value of  $T_h$  given in Table I. The values in the legend are in units of kelvin. The fixed parameters used for computing these results are found in Table I.

version never reaches zero due to zero point fluctuations. We point out, however, that the temperature of the hot reservoir as compared frequency of the hot filter is far lower than required for the classical limit, as evinced by the ratio  $\hbar\omega_h/(k_b T_h) \approx 1.7$ . Therefore, the thermal baths here need to be described by quantum noise.

## V. CONCLUSIONS

We proposed and theoretically analyzed a realistic superconducting quantum circuit capable of demonstrating the first autonomous quantum heat engine. To validate this, we developed an efficient quasiclassical non-Markovian model that proves the circuit can generate microwave photons arising purely from heat flow and non-linear internal dynamics.

The model enables us to estimate the photon generation rate, which directly translates to the output power. Our findings show that the generation rate can be relatively high — well within the observable range in circuit quantum electrodynamics — highlighting the feasibility of an experimental realization.

Unlike many theoretical works, we analyze a well-defined physical device, an electric circuit, and explicitly connect the theoretical model to its circuit parameters. The parameters were chosen such that they ensure experimental feasibility with modern fabrication techniques [57, 61, 65, 66], making this work a solid stepping stone toward autonomous thermal machines in cQED. Given the advancements in thermal devices and quantum thermodynamics within superconducting circuits [30, 38–42, 67], the realization of our proposed quantum heat engine appears to be only a matter of time. For high-power operation, exploring engineered environments [43, 68, 69], which have recently been shown to enable rapid thermal state preparation [70], could be an interesting direction for future research.

Furthermore, the output power was found to increase monotonically with the temperature of the hot reservoir, providing prospects for potential applications. We also compared the performance of the device when driven by classical noise instead of quantum noise and observed significant increase in the output power in the classical case. This observation attributed to the suppression of zero point fluctuations in the classical case. Our findings may provide insights into the limits and effects of low-temperature thermal environments governed by quantum mechanics, as opposed to classical thermal baths. In either case, our results pave the way for practical thermal machines in cQED, operating at cryogenic temperatures. For instance, the proposed device could serve as a coherent microwave photon source, harnessing thermal energy from temperature differences within a cryostat.

Even though our quasiclassical approach may lead to some loss of quantum character, we prioritized retaining the system’s non-linearity and non-Markovianity as key novelties of our method. While full quantization will undoubtedly introduce corrections to our classical estimates, it cannot eliminate the underlying phenomenon. Investigating the complete quantum nature of the device remains a topic for future work, but the results presented here serve as a significant and compelling proof of concept.

Beyond quantization, another promising theoretical direction would be extending the analysis of the non-linear coupling to a higher order. On the experimental side, it would be fruitful to explore various realizations of the proposed quantum heat engine and compare

their respective advantages and limitations. Finally, we point out that the presented approach does not directly provide an estimate of work fluctuations; however it should not be overlooked that phase and amplitude fluctuations in  $\phi_b$  are inherently present. Understanding and mitigating these fluctuations in the coherent output field of the heat engine calls for further studies.

## ACKNOWLEDGEMENTS

We acknowledge the support from the members of the QCD and PICO groups at Aalto University. Especially, we thank Jukka Pekola, Bayan Karimi, Christoforus Satria, Priyank Singh, Qiming Chen, Suman Kundu, and Rostislav Duda for fruitful scientific discourse and other help.

*a. Funding information* This work was funded by the Academy of Finland Centre of Excellence program (project Nos. 352925, and 336810) and grant Nos. 316619 and 349594 (THEPOW). We also acknowledge funding from the European Research Council under Advanced Grant No. 101053801 (ConceptQ).

## Appendix A: Deriving the optomechanical approximation

To handle the trigonometric potential in the SQUID Lagrangian, let us derive an approximation for it. Before expanding the trigonometric functions, however, let us analyze the potential energy related to the inductances in the SQUID loop. The potential energy is given as

$$U = \frac{(\varphi_g - \Phi_{\text{ext}})^2}{2L_g} - E_J \cos\left(\frac{2\pi\varphi_s}{\Phi_0}\right) - E_J \cos\left(\frac{2\pi}{\Phi_0}[\varphi_s - \varphi_g]\right), \quad (\text{A.1})$$

where we have chosen to rewrite the external flux,  $\Phi_{\text{ext}}$ , outside of the cosine, as can be done. Let us now find the potential minimum with respect to the fields  $\varphi_s$  and  $\varphi_g$ . By applying  $\partial U/\partial\varphi_s = 0$  and  $\partial U/\partial\varphi_g = 0$ , we find two conditions, the first simply being  $\varphi_s^0 = \varphi_g^0/2$ , and the second stating

$$\frac{\varphi_g^0 - \Phi_{\text{ext}}}{L_g} + \frac{2E_J\pi}{\Phi_0} \sin\left(\frac{\pi}{\Phi_0}\varphi_g^0\right) = 0. \quad (\text{A.2})$$

This is a transcendental equation that needs to be solved numerically. This does not matter as we will resort to numerics at the end anyhow.

Let us now assume a solution,  $\varphi_g^0$ , of the above equation. We apply a change of variable to the fields inductively coupled to the SQUID in order to shift the fields close to the potential minimum. We define new field variables as

$$\tilde{\varphi}_a = \varphi_a - \varphi_g^0/2, \quad \tilde{\varphi}_s = \varphi_s - \varphi_g^0/2 \quad (\text{A.3})$$

$$\tilde{\varphi}_b = \varphi_b - \varphi_g^0/2, \quad \tilde{\varphi}_g = \varphi_g - \varphi_g^0/2. \quad (\text{A.4})$$

Applying this to the SQUID Lagrangian, one obtains

$$\begin{aligned} \mathcal{L}_S &= -\frac{(\tilde{\varphi}_g + \varphi_g^0 - \Phi_{\text{ext}})^2}{2L_g} + E_J \cos\left(\frac{2\pi}{\Phi_0} [\tilde{\varphi}_s + \varphi_g^0/2]\right) + E_J \cos\left(\frac{2\pi}{\Phi_0} [\tilde{\varphi}_s - \tilde{\varphi}_g - \varphi_g^0/2]\right) \\ &= -\frac{(\tilde{\varphi}_g + \varphi_g^0 - \Phi_{\text{ext}})^2}{2L_g} + 2E_J \cos\left(\frac{\pi}{\Phi_0} [\tilde{\varphi}_g + \varphi_g^0]\right) \cos\left(\frac{\pi}{\Phi_0} [2\tilde{\varphi}_s - \tilde{\varphi}_g]\right). \end{aligned} \quad (\text{A.5})$$

Upon expanding the trigonometric functions with respect to  $\tilde{\varphi}_g$  and  $\tilde{\varphi}_s$ , we obtain

$$\begin{aligned} \cos\left(\frac{\pi}{\Phi_0} [\tilde{\varphi}_g + \varphi_g^0]\right) \cos\left(\frac{\pi}{\Phi_0} [2\tilde{\varphi}_s - \tilde{\varphi}_g]\right) &= \left[ \cos\left(\frac{\pi}{\Phi_0} \varphi_g^0\right) - \frac{\pi}{\Phi_0} \sin\left(\frac{\pi}{\Phi_0} \varphi_g^0\right) \tilde{\varphi}_g + \dots \right] \\ &\times \left\{ \left[ 1 - \frac{2\pi^2}{\Phi_0^2} \tilde{\varphi}_s^2 + \dots \right] \left[ 1 - \frac{\pi^2}{2\Phi_0^2} \tilde{\varphi}_g^2 + \dots \right] + \frac{2\pi^2}{\Phi_0^2} \tilde{\varphi}_s \tilde{\varphi}_g + \dots \right\}. \end{aligned} \quad (\text{A.6})$$

Next, we multiply open the parenthesis, truncate the expression to second order in field variables everywhere, and plug the result back into the Lagrangian. As we do this, we discover the left-hand-side of Eq. (A.2) multiplied by  $\tilde{\varphi}_g$  appearing in the Lagrangian. As this must be zero, we can safely drop it. Further, we will drop all constants, as they will not affect the equations of motion anyhow. The Lagrangian now reads

$$\begin{aligned} \mathcal{L}_S &= 2E_J \left[ -\frac{\pi^2}{\Phi_0^2} \cos\left(\frac{\pi}{\Phi_0} \varphi_g^0\right) \tilde{\varphi}_g^2 - \frac{2\pi^2}{\Phi_0^2} \cos\left(\frac{\pi}{\Phi_0} \varphi_g^0\right) \tilde{\varphi}_s^2 + \frac{2\pi^3}{\Phi_0^3} \sin\left(\frac{\pi}{\Phi_0} \varphi_g^0\right) \tilde{\varphi}_g \tilde{\varphi}_s^2 \right. \\ &\quad \left. + \frac{2\pi^2}{\Phi_0^2} \cos\left(\frac{\pi}{\Phi_0} \varphi_g^0\right) \tilde{\varphi}_g \tilde{\varphi}_s - \frac{2\pi^3}{\Phi_0^3} \sin\left(\frac{\pi}{\Phi_0} \varphi_g^0\right) \tilde{\varphi}_g^2 \tilde{\varphi}_s \right] - \frac{\tilde{\varphi}_g^2}{2L_g}, \end{aligned} \quad (\text{A.7})$$

Above, the first two terms in the brackets give inductive energy terms arising from the SQUID inductance. The third term is the optomechanical coupling, while the fourth and fifth terms are the linear and inverse optomechanical couplings. As a final step, we will drop the linear interaction term as well as the inverse optomechanical coupling, as they are assumed weak due to the large frequency offset between the modes  $\varphi_g$  and  $\varphi_s$ . This yields the approximated Lagrangian given by Eq. (3), where we have dropped the tildes for the sake of neat notation. All of the field variables in the main text after this approximation are in this shifted basis, however.

## Appendix B: Simplifying the equations of motion

As explained in the main text, our goal is to integrate out the field degrees of freedom  $\varphi_a$ ,  $\varphi_f$  and  $\varphi_g$ . We begin by solving  $\varphi_g$  from Eq. (7d) in time domain, which requires nothing but standard algebra. This solution is then inserted into the Eqs. (7b) and (7c), where the resulting third-order term ( $\sim \varphi_s^3$ ) is neglected, in accordance with the truncation of the series discussed in Appendix A. We thus eliminate  $\varphi_g$ , leaving us with four equations. The resulting form of Eq. (7c), governing the evolution of  $\varphi_b$ , readily matches the final shape of Eq. (10) in the main text. Consequently, we only need to combine the three remaining equations.

In order to derive Eq. (9) in the main text, we need to eliminate  $\varphi_f$  and  $\varphi_a$ . First, we solve Eq. (7e) for  $\varphi_f$  via Fourier transform, yielding

$$\hat{\varphi}_f = \frac{\hat{\xi}_f(\omega) + \kappa_f \omega^2 \hat{\varphi}_a}{\omega_f^2 - \omega^2 - 2i\gamma_f \omega}. \quad (\text{B.1})$$

We additionally Fourier transform Eq. (7a), and substitute the above solution in there, resulting in

$$-\omega^2 \hat{\varphi}_a + \omega_a^2 (\hat{\varphi}_a - \hat{\varphi}_s) - \omega^2 \sum_f \kappa_f \eta_f(\omega) \hat{\varphi}_a = \sum_f \eta_f(\omega) \xi_f(\omega) \quad (\text{B.2})$$

where we utilize the helper function  $\eta_f(\omega)$ , defined in the main text by Eq. (14). The above equation solves to

$$\hat{\varphi}_a = \frac{\omega_a^2 \hat{\varphi}_s + \sum_f \eta_f(\omega) \xi_f(\omega)}{\omega_a^2 - \omega^2 \left[ 1 + \sum_f \kappa_f \eta_f(\omega) \right]}. \quad (\text{B.3})$$

We further Fourier transform Eq. (7b) and insert the above solution into the obtained equation, finally yielding

$$[\omega_s^2 - \mathcal{K}(\omega)] \hat{\varphi}_s(\omega) - \frac{2g_0^2}{C_{\Sigma a} N_L} \chi(\omega) = \xi(\omega), \quad (\text{B.4})$$

where  $\chi(\omega)$  denotes the Fourier transform of  $\varphi_s(t)\varphi_b(t)$ , and the angular frequency  $\omega_s$ , the total memory kernel  $\mathcal{K}(\omega)$ , and the total noise source function  $\xi(\omega)$  are defined in the main text. Fourier transforming the above equation back to the time domain yields an equation of form Eq. (9) in the main text.

As a final step, we transform the field variables dimensionless. To this end, we write the field variable in a form  $\varphi_i = \sqrt{\hbar Z_i / 2x_i} \phi_i$ , where  $i=s, b$ ,  $Z_i$  is the characteristic impedance of



the resonator,  $\phi_i$  is the dimensionless field variable, and  $x_i$  is a dimensional scaling constant. We substitute  $\phi_i$  into the equations derived above, and find  $x_i$  such that the units match throughout the equation. We find  $x_i = \Phi_0/\pi\sqrt{2/(\hbar Z_i)}$ . With this, we finally write down the Eqs. (9) and (10) given in the main text.

### Appendix C: Numerical solution of the Green's function

To derive the Eq. (19) in the main text, we first utilize Eq. (17), where we expand the cosine in terms of exponential functions. Next, we use the Fourier transform of the Green's function, given by Eq. (18) in the main text. Simple substitution of these definitions yields

$$\begin{aligned} & \frac{1}{2\pi} \iint_{-\infty}^{\infty} [\omega_s^2 - \mathcal{K}(\omega)] G(\omega, \omega') e^{-i\omega t + i\omega' t'} d\omega d\omega' \\ & + \frac{2g_s^2 A_b}{2\pi} \iint_{-\infty}^{\infty} (e^{-i[(\omega_b + \omega)t + \theta]} + e^{i[(\omega_b - \omega)t + \theta]}) G(\omega, \omega') e^{i\omega' t'} d\omega d\omega' = \delta(t - t'), \end{aligned} \quad (\text{C.1})$$

where we neglect the time-dependence of  $A_b$  and  $\theta_b$ , as explained in the main text. A change variables ( $\omega_b \pm \omega \rightarrow \pm\omega$ ) on the latter row gives

$$\begin{aligned} & \frac{1}{2\pi} \iint_{-\infty}^{\infty} [\omega_s^2 - \mathcal{K}(\omega)] G(\omega, \omega') e^{-i\omega t + i\omega' t'} d\omega d\omega' \\ & + \frac{2g_s^2 A_b}{2\pi} \iint_{-\infty}^{\infty} [G(\omega - \omega_b, \omega') e^{-i\theta} + G(\omega + \omega_b, \omega') e^{i\theta}] e^{-i\omega t + i\omega' t'} d\omega d\omega' = \delta(t - t'). \end{aligned} \quad (\text{C.2})$$

To obtain Eq. (19), we Fourier transform the delta function on the right hand side and drop the Fourier integrals.

Next, we derive the matrix equation for the Green's function, Eq. (21). Upon inserting the series expansion of the Green's function, given by Eq. (20), into the Eq. (19), we obtain

$$\sum_n [P(\omega)G_n + R^*(\theta_b)G_{n-1} + R(\theta_b)G_{n+1}] \delta(\omega - \omega' - n\omega_b) = \delta(\omega - \omega'), \quad (\text{C.3})$$

where we shift the indexes of the two latter terms by one to write the terms under the same sum. Taking the integral over  $\omega$ , one finds the Eq. (21) given in the main text. This set of

equations can be written as a matrix equation:

$$\begin{pmatrix} \cdot & \cdot & \cdot & \cdot & \cdot & \cdot & \cdot \\ \cdot & P(\omega - 2\omega_b) & R(A_b, \theta_b) & 0 & 0 & 0 & \cdot \\ \cdot & R^*(A_b, \theta_b) & P(\omega - \omega_b) & R(A_b, \theta_b) & 0 & 0 & \cdot \\ \cdot & 0 & R^*(A_b, \theta_b) & P(\omega) & R(A_b, \theta_b) & 0 & \cdot \\ \cdot & 0 & 0 & R^*(A_b, \theta_b) & P(\omega + \omega_b) & R(A_b, \theta_b) & \cdot \\ \cdot & 0 & 0 & 0 & R^*(A_b, \theta_b) & P(\omega + 2\omega_b) & \cdot \\ \cdot & \cdot & \cdot & \cdot & \cdot & \cdot & \cdot \end{pmatrix} \begin{pmatrix} \cdot \\ G_{-2} \\ G_{-1} \\ G_0 \\ G_1 \\ G_2 \\ \cdot \end{pmatrix} = \begin{pmatrix} \cdot \\ 0 \\ 0 \\ 1 \\ 0 \\ 0 \\ \cdot \end{pmatrix}. \quad (\text{C.4})$$

Solving this matrix equation numerically is very efficient, since inverting the tridiagonal matrix found on the left hand side is a linear time operation in  $n$  [71]

Once the above matrix equation is solved to the desired degree in  $n$ , the Green's function can be expressed through Eq. (20) in frequency domain. This allows us to solve Eq. (9) for an arbitrary source  $\xi(t)$ . In general, the solution to a differential equation is given as a convolution of the Green's function with the source:

$$\phi_s(t) = \int_{-\infty}^{\infty} G(t', t) \xi(t') dt'. \quad (\text{C.5})$$

#### Appendix D: Noise and time averages

As explained in the main text, we want to compute the noise expectation value of  $\phi_a^2$ . Starting from the general solution of  $\phi_s$  obtained above, we express this as

$$\langle \phi_s^2 \rangle_{\xi}(t) = \left\langle \iint \int_{-\infty}^{\infty} G(t', t) \xi(t') G(t'', t) \xi(t'') dt' dt'' \right\rangle. \quad (\text{D.1})$$

Let us Fourier transform the noise functions and rearrange the expectation value to obtain

$$\langle \phi_s^2 \rangle_{\xi}(t) = \frac{1}{4\pi^2} \iiint \int_{-\infty}^{\infty} G(t', t) G(t'', t) \langle \xi(\omega') \xi(\omega'') \rangle e^{-i\omega' t'} e^{-i\omega'' t''} dt' dt'' d\omega' d\omega''. \quad (\text{D.2})$$

By the properties of the noise function, we know that the expectation value here is given as  $\langle \xi(\omega) \xi(\omega') \rangle = S(\omega) \delta(\omega + \omega')$ , where  $S(\omega)$  is the noise spectral density. Upon inserting this in and taking the  $\omega''$  integral, the above becomes

$$\langle \phi_s^2 \rangle_{\xi}(t) = \frac{1}{4\pi^2} \iint \int_{-\infty}^{\infty} G(t', t) G(t'', t) S(\omega') e^{-i\omega' t'} e^{i\omega' t''} dt' dt'' d\omega' \quad (\text{D.3})$$

where we use the property  $S(-\omega) = S(\omega)$  of the spectral density. Next, we shall insert the Fourier transform of the Green's function given by Eq. (18), yielding

$$\begin{aligned} \langle \phi_s^2 \rangle_\xi(t) &= \left( \frac{1}{4\pi^2} \right)^2 \int \cdots \int_{-\infty}^{\infty} G(\omega'', \omega) G(\tilde{\omega}, \tilde{\omega}') S(\omega') \\ &\times e^{-i\omega''t' + i\omega t} e^{-i\tilde{\omega}t'' + i\tilde{\omega}'t} e^{-i\omega't' + i\omega't''} dt' dt'' d\omega d\omega' d\omega'' d\tilde{\omega} d\tilde{\omega}' \end{aligned} \quad (\text{D.4})$$

Here we note that both  $t'$  and  $t''$  integrals can be used to yield Dirac delta functions. We first use the  $t'$  integral to produce  $\delta(\omega' + \omega'')$  and take the  $\omega''$  integral immediately. After this, we utilize the  $t''$  integral to produce  $\delta(\tilde{\omega} - \omega')$  and take the  $\tilde{\omega}$  integral. This finally yields

$$\langle \phi_s^2 \rangle_\xi(t) = \frac{1}{4\pi^2} \iint \int_{-\infty}^{\infty} G(-\omega', \omega) G(\omega', \tilde{\omega}') S(\omega') e^{it(\omega + \tilde{\omega}')} d\omega d\omega' d\tilde{\omega}'. \quad (\text{D.5})$$

As a result of the numerical solution of the Green's function, we want to express the above result in terms of the series representation of the Green's function. By direct substitution, we obtain

$$\begin{aligned} \langle \phi_a^2 \rangle_\xi &= \frac{1}{4\pi^2} \iint \int_{-\infty}^{\infty} \sum_{n,m} G_n(-\omega') G_m(\omega') \delta(-\omega' - \omega - n\omega_b) \delta(\omega' - \tilde{\omega}' - m\omega_b) \\ &\times S(\omega') e^{it(\omega + \tilde{\omega}')} d\omega d\omega' d\tilde{\omega}' \end{aligned} \quad (\text{D.6})$$

$$= \frac{1}{4\pi^2} \int_{-\infty}^{\infty} \sum_{n,m} G_n(-\omega') G_m(\omega') S(\omega') e^{-it(n+m)\omega_b} d\omega'. \quad (\text{D.7})$$

As a final step, let us foresightfully time-average the above expression over one period of oscillation of the mode  $\phi_b$ . Let us consider the Fourier harmonic resonant to the mode, so that the time-average reads

$$\begin{aligned} \langle \phi_a^2 \rangle_{\xi,t} &= \frac{\omega_b}{2\pi} \frac{1}{4\pi^2} \int_0^{2\pi/\omega_b} e^{i\omega_b t} \int_{-\infty}^{\infty} \sum_{n,m} G_n(-\omega) G_m(\omega) S(\omega) e^{-it(n+m)\omega_b} d\omega dt \\ &= \frac{\omega_b}{2\pi} \frac{1}{4\pi^2} \int_{-\infty}^{\infty} \sum_{nm} G_n(-\omega) G_m(\omega) S(\omega) \int_0^{2\pi/\omega_b} e^{-it(n+m-1)\omega_b} dt d\omega, \end{aligned} \quad (\text{D.8})$$

where we rearrange the formula such that we obtain the integral expression of Kronecker delta as given by the time-integral. With this, we simplify the result:

$$\begin{aligned} \langle \phi_a^2 \rangle_{\xi,t}(A_b, \theta_b) &= \frac{1}{4\pi^2} \int_{-\infty}^{\infty} \sum_{n,m} G_n(-\omega) G_m(\omega) S(\omega) \delta_{m,-n+1} d\omega \\ &= \frac{1}{4\pi^2} \int_{-\infty}^{\infty} \sum_n G_n(\omega) G_{n-1}^*(\omega) S(\omega) d\omega, \end{aligned} \quad (\text{D.9})$$

where we use  $G_{-n}(-\omega) = G_n^*(\omega)$ . We now have a function of  $A_b$  and  $\theta_b$  describing the average noise pressure on the mode  $\phi_b$ .

As mentioned in the main text, in order to derive the equations of motion for the amplitude and phase of the mode  $\phi_b$ , we once again use  $\phi_b(t) = A_b(t) (e^{-i[\omega_b t + \theta_b(t)]} + e^{i[\omega_b t + \theta_b(t)]})$ . The derivatives then read

$$\dot{\theta}_b(t) = \dot{A}_b(t)e^{-i[\omega_b t + \theta_b(t)]} - iA_b(t)[\omega_b + \dot{\theta}_b(t)]e^{-i[\omega_b t + \theta_b(t)]} + c.c. \quad (D.10)$$

$$\begin{aligned} \ddot{\phi}_g(t) = & \ddot{A}_b(t)e^{-i[\omega_b t + \theta_b(t)]} - 2i\dot{A}_b(t)[\omega_b + \dot{\theta}_b(t)]e^{-i[\omega_b t + \theta_b(t)]} \\ & - iA_b(t)\ddot{\theta}_b(t)e^{-i[\omega_b t + \theta_b(t)]} - A_b(t)[\omega_b + \dot{\theta}_b(t)]^2e^{-i[\omega_b t + \theta_b(t)]} + c.c. \end{aligned} \quad (D.11)$$

In the spirit of the WKB approximation, let us immediately drop the second derivatives, products and powers of derivatives, and the terms  $\gamma_b \dot{A}_b$  and  $\gamma_b \dot{\theta}_b$ . Upon inserting the Fourier component shown above of remaining expressions into Eq. (23) we obtain

$$\left[ -2i\omega_b \dot{A}_b(t) - 2\omega_b A_b(t) \dot{\theta}_b(t) - 2i\gamma_b A_b \omega_b \right] e^{-i[\omega_b t + \theta_b(t)]} - g_b^2 \langle \phi_a^2 \rangle_{\xi} (A_b, \theta_b) = 0. \quad (D.12)$$

The reason for computing the time-average above now becomes apparent: multiplying this equation by  $e^{i[\omega_b t + \theta_b(t)]}$  and time-averaging over the whole equation gives the exact term computed above multiplied by  $e^{i\theta_b(t)}$ . Decomposing this results into the real and imaginary parts gives

$$A_b(t) \dot{\theta}_b + \frac{g_b^2}{2\omega_b} \text{Re}[\langle \phi_a^2 \rangle_{\xi, t} (A_b, \theta_b) e^{i\theta_b(t)}] = 0 \quad (D.13)$$

$$\dot{A}_b(t) + \gamma_b A_b + \frac{g_b^2}{2\omega_b} \text{Im}[\langle \phi_a^2 \rangle_{\xi, t} (A_b, \theta_b) e^{i\theta_b(t)}] = 0. \quad (D.14)$$

In the expression given in the main text Eq. (26) the phase exponent  $e^{i\theta_b(t)}$  has been included in the definition of  $\langle \phi_a^2 \rangle_{\xi, t} (A_b, \theta_b)$ .

- 
- [1] W. P. Schleich, K. S. Ranade, C. Anton, M. Arndt, M. Aspelmeyer, M. Bayer, G. Berg, T. Calarco, E. Fuchs, Haraldand Giacobino, M. Grassl, W. M. Hänggi, Peterand Heckl, I.-V. Hertel, S. Huelga, F. Jelezko, B. Keimer, J. P. Kotthaus, G. Leuchs, N. Lütkenhaus, T. Maurer, Ueliand Pfau, M. B. Plenio, E. M. Rasel, O. Renn, C. Silberhorn, J. Schiedmayer, D. Schmitt-Landsiedel, K. Schönhammer, A. Ustinov, P. Walther, H. Weinfurter, E. Welzl, R. Wiesendanger, S. Wolf, A. Zeilinger, and P. Zoller, Quantum technology: from research to application, Applied Physics B **122**, 130 (2016).

- [2] P. Krantz, M. Kjaergaard, F. Yan, T. P. Orlando, S. Gustavsson, and W. D. Oliver, A quantum engineer's guide to superconducting qubits, *Applied Physics Reviews* **6**, 021318 (2019), [https://pubs.aip.org/aip/apr/article-pdf/doi/10.1063/1.5089550/16667201/021318.1\\_online.pdf](https://pubs.aip.org/aip/apr/article-pdf/doi/10.1063/1.5089550/16667201/021318.1_online.pdf).
- [3] L. DiCarlo, J. M. Chow, J. M. Gambetta, L. S. Bishop, B. R. Johnson, D. I. Schuster, J. Majer, A. Blais, L. Frunzio, S. M. Girvin, and R. J. Schoelkopf, Demonstration of two-qubit algorithms with a superconducting quantum processor, *Nature* **460**, 240 (2009).
- [4] E. Lucero, R. Barends, Y. Chen, J. Kelly, M. Mariantoni, A. Megrant, P. O'Malley, D. Sank, A. Vainsencher, J. Wenner, T. White, Y. Yin, A. N. Cleland, and J. M. Martinis, Computing prime factors with a josephson phase qubit quantum processor, *Nature Physics* **8**, 719 (2012).
- [5] Y. Zheng, C. Song, M.-C. Chen, B. Xia, W. Liu, Q. Guo, L. Zhang, D. Xu, H. Deng, K. Huang, Y. Wu, Z. Yan, D. Zheng, L. Lu, J.-W. Pan, H. Wang, C.-Y. Lu, and X. Zhu, Solving systems of linear equations with a superconducting quantum processor, *Phys. Rev. Lett.* **118**, 210504 (2017).
- [6] M.-C. Chen, M. Gong, X. Xu, X. Yuan, J.-W. Wang, C. Wang, C. Ying, J. Lin, Y. Xu, Y. Wu, S. Wang, H. Deng, F. Liang, C.-Z. Peng, S. C. Benjamin, X. Zhu, C.-Y. Lu, and J.-W. Pan, Demonstration of adiabatic variational quantum computing with a superconducting quantum coprocessor, *Phys. Rev. Lett.* **125**, 180501 (2020).
- [7] M. P. Harrigan, K. J. Sung, M. Neeley, K. J. Satzinger, F. Arute, K. Arya, J. Atalaya, J. C. Bardin, R. Barends, S. Boixo, M. Broughton, B. B. Buckley, D. A. Buell, B. Burkett, N. Bushnell, Y. Chen, Z. Chen, B. Chiaro, R. Collins, W. Courtney, S. Demura, A. Dunsworth, D. Eppens, A. Fowler, B. Foxen, C. Gidney, M. Giustina, R. Graff, S. Habegger, A. Ho, S. Hong, T. Huang, L. B. Ioffe, S. V. Isakov, E. Jeffrey, Z. Jiang, C. Jones, D. Kafri, K. Kechedzhi, J. Kelly, S. Kim, P. V. Klimov, A. N. Korotkov, F. Kostritsa, D. Landhuis, P. Laptev, M. Lindmark, M. Leib, O. Martin, J. M. Martinis, J. R. McClean, M. McEwen, A. Megrant, X. Mi, M. Mohseni, W. Mruczkiewicz, J. Mutus, O. Naaman, C. Neill, F. Neukart, M. Y. Niu, T. E. O'Brien, B. O'Gorman, E. Ostby, A. Petukhov, H. Putterman, C. Quintana, P. Roushan, N. C. Rubin, D. Sank, A. Skolik, V. Smelyanskiy, D. Strain, M. Streif, M. Szalay, A. Vainsencher, T. White, Z. J. Yao, P. Yeh, A. Zalcman, L. Zhou, H. Neven, D. Bacon, E. Lucero, E. Farhi, and R. Babbush, Quantum approximate optimization of non-planar graph problems on a planar superconducting processor, *Nature Physics* **17**, 332 (2021).

- [8] C. J. Axline, L. D. Burkhardt, W. Pfaff, M. Zhang, K. Chou, P. Campagne-Ibarcq, P. Reinhold, L. Frunzio, S. M. Girvin, L. Jiang, M. H. Devoret, and R. J. Schoelkopf, On-demand quantum state transfer and entanglement between remote microwave cavity memories, *Nature Physics* **14**, 705 (2018).
- [9] P. Kurpiers, P. Magnard, T. Walter, B. Royer, M. Pechal, J. Heinsoo, Y. Salathé, A. Akin, S. Storz, J.-C. Besse, S. Gasparinetti, A. Blais, and A. Wallraff, Deterministic quantum state transfer and remote entanglement using microwave photons, *Nature* **558**, 264 (2018).
- [10] S. Pogorzalek, K. G. Fedorov, M. Xu, A. Parra-Rodriguez, M. Sanz, M. Fischer, E. Xie, K. Inomata, Y. Nakamura, E. Solano, A. Marx, F. Deppe, and R. Gross, Secure quantum remote state preparation of squeezed microwave states, *Nature Communications* **10**, 2604 (2019).
- [11] K. G. Fedorov, M. Renger, S. Pogorzalek, R. D. Candia, Q. Chen, Y. Nojiri, K. Inomata, Y. Nakamura, M. Partanen, A. Marx, R. Gross, and F. Deppe, Experimental quantum teleportation of propagating microwaves, *Science Advances* **7**, eabk0891 (2021), <https://www.science.org/doi/pdf/10.1126/sciadv.abk0891>.
- [12] D. L. Underwood, W. E. Shanks, J. Koch, and A. A. Houck, Low-disorder microwave cavity lattices for quantum simulation with photons, *Phys. Rev. A* **86**, 023837 (2012).
- [13] A. A. Abdumalikov Jr, J. M. Fink, K. Juliusson, M. Pechal, S. Berger, A. Wallraff, and S. Filipp, Experimental realization of non-abelian non-adiabatic geometric gates, *Nature* **496**, 482 (2013).
- [14] P. Roushan, C. Neill, A. Megrant, Y. Chen, R. Babbush, R. Barends, B. Campbell, Z. Chen, B. Chiaro, A. Dunsworth, A. Fowler, E. Jeffrey, J. Kelly, E. Lucero, J. Mutus, P. J. J. O'Malley, M. Neeley, C. Quintana, D. Sank, A. Vainsencher, J. Wenner, T. White, E. Kapit, H. Neven, and J. Martinis, Chiral ground-state currents of interacting photons in a synthetic magnetic field, *Nature Physics* **13**, 146 (2017).
- [15] A. J. Kollár, M. Fitzpatrick, and A. A. Houck, Hyperbolic lattices in circuit quantum electrodynamics, *Nature* **571**, 45 (2019).
- [16] R. Ma, B. Saxberg, C. Owens, N. Leung, Y. Lu, J. Simon, and D. I. Schuster, A dissipatively stabilized mott insulator of photons, *Nature* **566**, 51 (2019).
- [17] K. Xu, Z.-H. Sun, W. Liu, Y.-R. Zhang, H. Li, H. Dong, W. Ren, P. Zhang, F. Nori, D. Zheng, H. Fan, and H. Wang, Probing dynamical phase transitions

- with a superconducting quantum simulator, *Science Advances* **6**, eaba4935 (2020), <https://www.science.org/doi/pdf/10.1126/sciadv.aba4935>.
- [18] Q. Guo, C. Cheng, Z.-H. Sun, Z. Song, H. Li, Z. Wang, W. Ren, H. Dong, D. Zheng, Y.-R. Zhang, R. Mondaini, H. Fan, and H. Wang, Observation of energy-resolved many-body localization, *Nature Physics* **17**, 234 (2021).
- [19] Q.-M. Chen, M. Fischer, Y. Nojiri, M. Renger, E. Xie, M. Partanen, S. Pogorzalek, K. G. Fedorov, A. Marx, F. Deppe, and R. Gross, Quantum behavior of the duffing oscillator at the dissipative phase transition, *Nature Communications* **14**, 2896 (2023).
- [20] S. Barzanjeh, S. Pirandola, D. Vitali, and J. M. Fink, Microwave quantum illumination using a digital receiver, *Science Advances* **6**, eabb0451 (2020), <https://www.science.org/doi/pdf/10.1126/sciadv.abb0451>.
- [21] A. Bienfait, P. Campagne-Ibarcq, A. H. Küllerich, X. Zhou, S. Probst, J. J. Pla, T. Schenkel, D. Vion, D. Esteve, J. J. L. Morton, K. Moelmer, and P. Bertet, Magnetic resonance with squeezed microwaves, *Phys. Rev. X* **7**, 041011 (2017).
- [22] Z. Wang, M. Xu, X. Han, W. Fu, S. Puri, S. M. Girvin, H. X. Tang, S. Shankar, and M. H. Devoret, Quantum microwave radiometry with a superconducting qubit, *Phys. Rev. Lett.* **126**, 180501 (2021).
- [23] R. Kokkonen, J. Govenius, V. Vesterinen, R. E. Lake, A. M. Gunyhó, K. Y. Tan, S. Simbierowicz, L. Grönberg, J. Lehtinen, M. Prunnila, J. Hassel, A. Lamminen, O.-P. Saira, and M. Möttönen, Nanobolometer with ultralow noise equivalent power, *Communications Physics* **2**, 124 (2019).
- [24] R. Kokkonen, J.-P. Girard, D. Hazra, A. Laitinen, J. Govenius, R. E. Lake, I. Sallinen, V. Vesterinen, M. Partanen, J. Y. Tan, K. W. Chan, K. Y. Tan, P. Hakonen, and M. Möttönen, Bolometer operating at the threshold for circuit quantum electrodynamics, *Nature* **586**, 47 (2020).
- [25] J. Govenius, R. E. Lake, K. Y. Tan, and M. Möttönen, Detection of zeptojoule microwave pulses using electrothermal feedback in proximity-induced josephson junctions, *Phys. Rev. Lett.* **117**, 030802 (2016).
- [26] S. Gasparinetti, K. L. Viisanen, O.-P. Saira, T. Faivre, M. Arzeo, M. Meschke, and J. P. Pekola, Fast electron thermometry for ultrasensitive calorimetric detection, *Phys. Rev. Appl.* **3**, 014007 (2015).

- [27] S. Deffner and S. Campbell, *Quantum Thermodynamics*, 2053-2571 (Morgan and Claypool Publishers, 2019).
- [28] J. Goold, M. Huber, A. Riera, L. del Rio, and P. Skrzypczyk, The role of quantum information in thermodynamics—a topical review, *Journal of Physics A: Mathematical and Theoretical* **49**, 143001 (2016).
- [29] J. Gemmer, M. Michel, and G. Mahler, *Quantum Thermodynamics: Emergence of Thermodynamic Behavior Within Composite Quantum Systems*, Lecture Notes in Physics (Springer Berlin Heidelberg, 2004).
- [30] S. Sundelin, M. A. Aamir, V. M. Kulkarni, C. Castillo-Moreno, and S. Gasparinetti, Quantum refrigeration powered by noise in a superconducting circuit (2024), arXiv:2403.03373 [quant-ph].
- [31] J. Roßnagel, S. T. Dawkins, K. N. Tolazzi, O. Abah, E. Lutz, F. Schmidt-Kaler, and K. Singer, A single-atom heat engine, *Science* **352**, 325 (2016), arXiv:1510.03681 [cond-mat.stat-mech].
- [32] D. von Lindenfels, O. Gräß, C. T. Schmiegelow, V. Kaushal, J. Schulz, M. T. Mitchison, J. Goold, F. Schmidt-Kaler, and U. G. Poschinger, Spin heat engine coupled to a harmonic-oscillator flywheel, *Phys. Rev. Lett.* **123**, 080602 (2019).
- [33] N. Van Horne, D. Yum, T. Dutta, P. Hänggi, J. Gong, D. Poletti, and M. Mukherjee, Single-atom energy-conversion device with a quantum load, *npj Quantum Information* **6**, 37 (2020).
- [34] J. Klatzow, J. N. Becker, P. M. Ledingham, C. Weinzetl, K. T. Kaczmarek, D. J. Saunders, J. Nunn, I. A. Walmsley, R. Uzdin, and E. Poem, Experimental demonstration of quantum effects in the operation of microscopic heat engines, *Phys. Rev. Lett.* **122**, 110601 (2019).
- [35] R. J. de Assis, T. M. de Mendonça, C. J. Villas-Boas, A. M. de Souza, R. S. Sarthour, I. S. Oliveira, and N. G. de Almeida, Efficiency of a quantum otto heat engine operating under a reservoir at effective negative temperatures, *Phys. Rev. Lett.* **122**, 240602 (2019).
- [36] J. P. S. Peterson, T. B. Batalhão, M. Herrera, A. M. Souza, R. S. Sarthour, I. S. Oliveira, and R. M. Serra, Experimental characterization of a spin quantum heat engine, *Phys. Rev. Lett.* **123**, 240601 (2019).
- [37] Q. Bouton, J. Nettersheim, S. Burgardt, D. Adam, E. Lutz, and A. Widera, A quantum heat engine driven by atomic collisions, *Nature Communications* **12**, 2063 (2021).
- [38] J. P. Pekola and F. W. J. Hekking, Normal-metal-superconductor tunnel junction as a brownian refrigerator, *Phys. Rev. Lett.* **98**, 210604 (2007).



- [39] J. P. Pekola, Towards quantum thermodynamics in electronic circuits, *Nature Physics* **11**, 118 (2015).
- [40] B. Karimi and J. P. Pekola, Otto refrigerator based on a superconducting qubit: Classical and quantum performance, *Phys. Rev. B* **94**, 184503 (2016).
- [41] G. Thomas, A. Gubaydullin, D. S. Golubev, and J. P. Pekola, Thermally pumped on-chip maser, *Phys. Rev. B* **102**, 104503 (2020).
- [42] A. Ronzani, B. Karimi, J. Senior, Y.-C. Chang, J. T. Peltonen, C. Chen, and J. P. Pekola, Tunable photonic heat transport in a quantum heat valve, *Nature Physics* **14**, 991 (2018).
- [43] K. Y. Tan, M. Partanen, R. E. Lake, J. Govenius, S. Masuda, and M. Möttönen, Quantum-circuit refrigerator, *Nature Communications* **8**, 15189 (2017).
- [44] M. Rasola and M. Möttönen, Autonomous quantum heat engine based on non-markovian dynamics of an optomechanical hamiltonian, *Scientific Reports* **14**, 9448 (2024).
- [45] S. Barzanjeh, A. Xuereb, S. Groblacher, M. Paternostro, C. A. Regal, and E. M. Weig, Optomechanics for quantum technologies, *Nature Physics* **18**, 15 (2022).
- [46] M. Aspelmeyer, T. J. Kippenberg, and F. Marquardt, Cavity optomechanics, *Rev. Mod. Phys.* **86**, 1391 (2014).
- [47] Y. Dong, K. Zhang, F. Bariani, and P. Meystre, Work measurement in an optomechanical quantum heat engine, *Phys. Rev. A* **92**, 033854 (2015).
- [48] K. Zhang, F. Bariani, and P. Meystre, Quantum optomechanical heat engine, *Phys. Rev. Lett.* **112**, 150602 (2014).
- [49] K. Zhang, F. Bariani, and P. Meystre, Theory of an optomechanical quantum heat engine, *Phys. Rev. A* **90**, 023819 (2014).
- [50] M. T. Naseem and Özgür E. Müstecaplıoğlu, Quantum heat engine with a quadratically coupled optomechanical system, *J. Opt. Soc. Am. B* **36**, 3000 (2019).
- [51] M. Izadyari, M. Öncü, K. Durak, and Özgür E. Müstecaplıoğlu, Quantum signatures in a quadratic optomechanical heat engine with an atom in a tapered trap, *J. Opt. Soc. Am. B* **39**, 3247 (2022).
- [52] A. U. C. Hardal, N. Aslan, C. M. Wilson, and O. E. Müstecaplıoğlu, Quantum heat engine with coupled superconducting resonators, *Phys. Rev. E* **96**, 062120 (2017).
- [53] A. Mari, A. Farace, and V. Giovannetti, Quantum optomechanical piston engines powered by heat, *Journal of Physics B: Atomic, Molecular and Optical Physics* **48**, 175501 (2015).

- [54] D. Gelbwaser-Klimovsky and G. Kurizki, Work extraction from heat-powered quantized optomechanical setups, *Scientific Reports* **5**, 7809 (2015).
- [55] D. Gelbwaser-Klimovsky, R. Alicki, and G. Kurizki, Work and energy gain of heat-pumped quantized amplifiers, *Europhysics Letters* **103**, 60005 (2013).
- [56] M. H. Devoret, *Quantum fluctuations in electrical circuits* (Edition de Physique, France, 1997).
- [57] U. Vool and M. Devoret, Introduction to quantum electromagnetic circuits, *International Journal of Circuit Theory and Applications* **45**, 897 (2017), <https://onlinelibrary.wiley.com/doi/pdf/10.1002/cta.2359>.
- [58] R. Kosloff and Y. Rezek, The quantum harmonic otto cycle, *Entropy* **19**, 10.3390/e19040136 (2017).
- [59] B. Hall, *Quantum Theory for Mathematicians*, Graduate Texts in Mathematics (Springer New York, 2013).
- [60] A. Schmid, On a quasiclassical langevin equation, *Journal of Low Temperature Physics* **49**, 609 (1982).
- [61] M. Göppl, A. Fragner, M. Baur, R. Bianchetti, S. Filipp, J. M. Fink, P. J. Leek, G. Puebla, L. Steffen, and A. Wallraff, Coplanar waveguide resonators for circuit quantum electrodynamics, *Journal of Applied Physics* **104**, 113904 (2008), <https://doi.org/10.1063/1.3010859>.
- [62] L. Frunzio, A. Wallraff, D. Schuster, J. Majer, and R. Schoelkopf, Fabrication and characterization of superconducting circuit qed devices for quantum computation, *IEEE Transactions on Applied Superconductivity* **15**, 860 (2005).
- [63] R. Barends, J. J. A. Baselmans, J. N. Hovenier, J. R. Gao, S. J. C. Yates, T. M. Klapwijk, and H. F. C. Hoevers, Niobium and tantalum high q resonators for photon detectors, *IEEE Transactions on Applied Superconductivity* **17**, 263 (2007).
- [64] E. V. Zikiy, A. I. Ivanov, N. S. Smirnov, D. O. Moskalev, A. R. Polozov, V. I. and Matanin, E. I. Malevannaya, V. V. Echeistov, T. G. Konstantinova, and I. A. Rodionov, High-q trenched aluminum coplanar resonators with an ultrasonic edge microcutting for superconducting quantum devices, *Scientific Reports* **13**, 15536 (2023).
- [65] M. Rasola, S. Klaver, J. Ma, P. Singh, T. Uusnäkki, H. Suominen, and M. Möttönen, Low-characteristic-impedance superconducting tadpole resonators in the sub-gigahertz regime, *Phys. Rev. Res.* **6**, 043297 (2024).

- [66] A. Blais, A. L. Grimsmo, S. M. Girvin, and A. Wallraff, Circuit quantum electrodynamics, *Rev. Mod. Phys.* **93**, 025005 (2021).
- [67] J. Pekola and I. Khaymovich, Thermodynamics in single-electron circuits and superconducting qubits, *Annual Review of Condensed Matter Physics* **10**, 193 (2019), <https://doi.org/10.1146/annurev-conmatphys-033117-054120>.
- [68] T. F. Mörstedt, A. Viitanen, V. Vadimov, V. Sevriuk, M. Partanen, E. Hyppä, G. Catelani, M. Silveri, K. Y. Tan, and M. Möttönen, Recent developments in quantum-circuit refrigeration, *Annalen der Physik* **534**, 2100543 (2022), <https://onlinelibrary.wiley.com/doi/pdf/10.1002/andp.202100543>.
- [69] A. Viitanen, T. Mörstedt, W. S. Teixeira, M. Tiiri, J. Rabinä, M. Silveri, and M. Möttönen, Quantum-circuit refrigeration of a superconducting microwave resonator well below a single quantum, *Phys. Rev. Res.* **6**, 023262 (2024).
- [70] T. F. Mörstedt, W. S. Teixeira, A. Viitanen, H. Kivijärvi, M. Tiiri, M. Rasola, A. M. Gunyho, S. Kundu, L. Lattier, V. Vadimov, G. Catelani, V. Sevriuk, J. Heinsoo, J. Rabinä, J. Ankerhold, and M. Möttönen, Rapid on-demand generation of thermal states in superconducting quantum circuits (2024), arXiv:2402.09594 [quant-ph].
- [71] B. Datta, *Numerical Linear Algebra and Applications: Second Edition*, Other Titles in Applied Mathematics (Society for Industrial and Applied Mathematics (SIAM, 3600 Market Street, Floor 6, Philadelphia, PA 19104), 2010).